

Magnetic anisotropy and entropy change in trigonal Cr₅Te₈

Yu Liu,¹ Milinda Abeykoon,² Eli Stavitski,² Klaus Attenkofer,² and C. Petrovic¹

¹Condensed Matter Physics and Materials Science Department,
Brookhaven National Laboratory, Upton, New York 11973, USA

²National Synchrotron Light Source II, Brookhaven National Laboratory, Upton, New York 11973, USA

(Dated: November 27, 2019)

We present a comprehensive investigation on anisotropic magnetic and magnetocaloric properties of the quasi-two-dimensional weak itinerant ferromagnet trigonal Cr₅Te₈ single crystals. Magnetic-anisotropy-induced satellite transition T^* is observed at low fields applied parallel to the ab plane below the Curie temperature ($T_c \sim 230$ K). T^* is featured by an anomalous magnetization downturn, similar to that in structurally related CrI₃, which possibly stems from an in-plane antiferromagnetic alignment induced by out-of-plane ferromagnetic spins canting. Magnetocrystalline anisotropy is also reflected in magnetic entropy change $\Delta S_M(T, H)$ and relative cooling power RCP. Given the high Curie temperature, Cr₅Te₈ crystals are materials of interest for nanofabrication in basic science and applied technology.

I. INTRODUCTION

Achieving long-range magnetism at low dimensions as well as high temperature is of great importance for the development of next-generation spintronics. As stated in the Mermin-Wagner theorem,¹ materials with isotropic Heisenberg interactions can not magnetically order in the two-dimensional (2D) limit. Strong magnetic anisotropy such as exchange anisotropy and/or single-ion anisotropy may remove this restriction. Recently, 2D long-range ferromagnetism was observed in van der Waals (vdW) CrI₃ and Cr₂Ge₂Te₆,²⁻⁸ however the Curie temperature T_c is significantly lowered when reducing to monolayer or few layers. The corresponding T_c in monolayer and bilayer was only ~ 45 K for CrI₃ and 25 K in Cr₂Ge₂Te₆, respectively. Therefore, high- T_c ferromagnets with strong anisotropy are highly desirable.

Binary chromium tellurides Cr_{1-x}Te are such promising candidates with high- T_c ranging from 170 to 360 K depending on different Cr vacancies.⁹⁻¹³ The carriers of magnetism in CrI₃ and Cr₂Ge₂Te₆ are Cr³⁺ ions with spin $S = 3/2$ which are octahedrally coordinated by Te ligands and form a honeycomb magnetic lattice in the ab plane. Cr_{1-x}Te crystallizes in a defective NiAs structure, showing similarities in crystal structure, magnetic ion, and magnetic ordering. The mechanism of FM in this system could be attributed to the dominant FM superexchange coupling between half-filled Cr t_{2g} and empty e_g states via Te p orbitals, against the AFM direct exchange interactions of Cr t_{2g} states. The saturation magnetization in Cr_{1-x}Te is observed as $1.7 \sim 2.5 \mu_B$, which is much smaller than the expected moment value of Cr using ionic model due to the spin canting, itinerant nature of the d electrons and the existence of mixed valence Cr.¹⁴ The electronic structure of Cr_{1-x}Te has further been studied by photoemission spectroscopy,¹⁵ showing the importance of electron-correlation effect. Here we focus on trigonal Cr₅Te₈ with $x = 0.375$, which has a higher T_c of 230 K compared with monoclinic space group.¹⁶⁻²⁰ Strong magnetic anisotropy with out-of-plane easy c axis has been confirmed.¹¹ Critical behavior analysis of trig-

onal Cr₅Te₈ illustrates that the ferromagnetic state below T_c conforms to three-dimensional (3D) Ising model,¹⁹ holding a high potential for establishing long-range magnetic order when thinned down to 2D limit. Anisotropic anomalous Hall effect (AHE) was recently observed in trigonal Cr₅Te₈.^{20,21} Calculations of band structure is desired to explain its origin, calling for precise structural information.

Magnetocaloric effect (MCE) in the FM vdW materials provides important insight into the magnetic properties. The magnetocrystalline anisotropy constant K_u is found to be larger for Cr₂Si₂Te₆ when compared to Cr₂Ge₂Te₆, resulting in larger rotational magnetic entropy change at T_c .²² CrI₃ also exhibits anisotropic $-\Delta S_M^{max}$ with values of 4.24 and 2.68 J kg⁻¹ K⁻¹ at 5 T for $\mathbf{H} \parallel \mathbf{c}$ and $\mathbf{H} \parallel \mathbf{ab}$, respectively.²³ Intriguingly, there is an anisotropic magnetic anomaly T^* just below T_c in low fields;^{2,23} the origin of T^* is still unknown.

In this work we investigate the anisotropy of magnetic and magnetocaloric properties in trigonal Cr₅Te₈ single crystal. A satellite transition T^* below T_c was observed, at which the huge magnetic anisotropy emerges. We assign its origin to the interplay among magnetocrystalline anisotropy, temperature and magnetic field. Whereas the anisotropic magnetic entropy change ΔS_M in Cr₅Te₈ is small, the magnetocrystalline anisotropy constant K_u is found to be temperature-dependent and comparable with CrI₃ and Cr₂Ge₂Te₆. As a result of high- T_c in Cr₅Te₈, it would be of interest to design low-dimensional FM heterostructures.

II. EXPERIMENTAL DETAILS

Plate-like single crystals of Cr₅Te₈ were fabricated by the self-flux method and the surface is the ab plane.^{19,20} The structure was characterized by powder x-ray diffraction (XRD) in the transmission mode at 28-D-1 beamline of the National Synchrotron Light Source II (NSLS II) at Brookhaven National Laboratory (BNL). Data were collected using a 0.5 mm² beam with wavelength $\lambda \sim 0.1668$

TABLE I. Structural parameters for Cr_5Te_8 obtained from synchrotron powder XRD at room temperature.

Chemical formula		Cr_5Te_8				
Space group		$P\bar{3}m1$				
a (Å)		7.7951				
c (Å)		11.9766				
atom	site	x	y	z	Occ.	U_{iso} (Å ²)
Cr	Cr1	0	0	0	0.87	0.0019
Cr	Cr2	0.4920	0.5080	0.2515	1	0.0019
Cr	Cr3	0	0	0.2747	1	0.0019
Cr	Cr4	0.5	0	0.5	0.264	0.0019
Te	Te1	0.3333	0.6667	0.1164	1	0.00468
Te	Te2	0.3333	0.6667	0.6217	1	0.00468
Te	Te3	0.1652	0.8348	0.3816	1	0.00468
Te	Te4	0.8285	0.1715	0.1301	1	0.00468

Å. A Perkin Elmer 2D detector (200×200 microns) was placed orthogonal to the beam path 990 mm away from the sample. The x-ray absorption spectroscopy measurement was performed at 8-ID beamline of NSLS II (BNL) in fluorescence mode. The x-ray absorption near edge structure (XANES) and the extended x-ray absorption fine structure (EXAFS) spectra were processed using the Athena software package. The extracted EXAFS signal, $\chi(k)$, was weighed by k^2 to emphasize the high-energy oscillation and then Fourier-transformed in a k range from 2 to 12 Å⁻¹ to analyze the data in R space. The magnetization data as a function of temperature and field were collected using Quantum Design MPMS-XL5 system in temperature range 200 ~ 280 K with a step of 4 K on cleaved crystals in order to remove surface contamination of residual Te flux droplets on the surface.

III. RESULTS AND DISCUSSION

Rietveld powder diffraction analysis was carried out on data obtained from the raw 2D diffraction data integrated and converted to intensity versus Q using the Fit2d software where $Q = 4\pi\sin\theta/\lambda$ is the magnitude of the scattering vector.²⁴ The refinement was performed using GSAS-II modeling suite.²⁵ Figure 1(a) shows the refinement result (goodness of fit ~ 4%) of Cr_5Te_8 (0.885 by weight) and residual Te flux impurity (0.115 by weight). The crystal structure of trigonal Cr_5Te_8 can be well refined in the $P\bar{3}m1$ space group with four crystallographically different sites for both Cr and Te atoms, leading to the formation of a five-layer superstructure of the CdI_2 type.²⁶ The detailed structural parameters are summarized in Table I. The superstructure is composed of three types of Cr layers with a stacking sequence abcba. Cr2 and Cr3 occupy the vacancy-free atomic layers, while Cr1 and Cr4 distribute in the metal-deficient layers [inset in Fig. 1(b)]. The average Cr-Te bond dis-

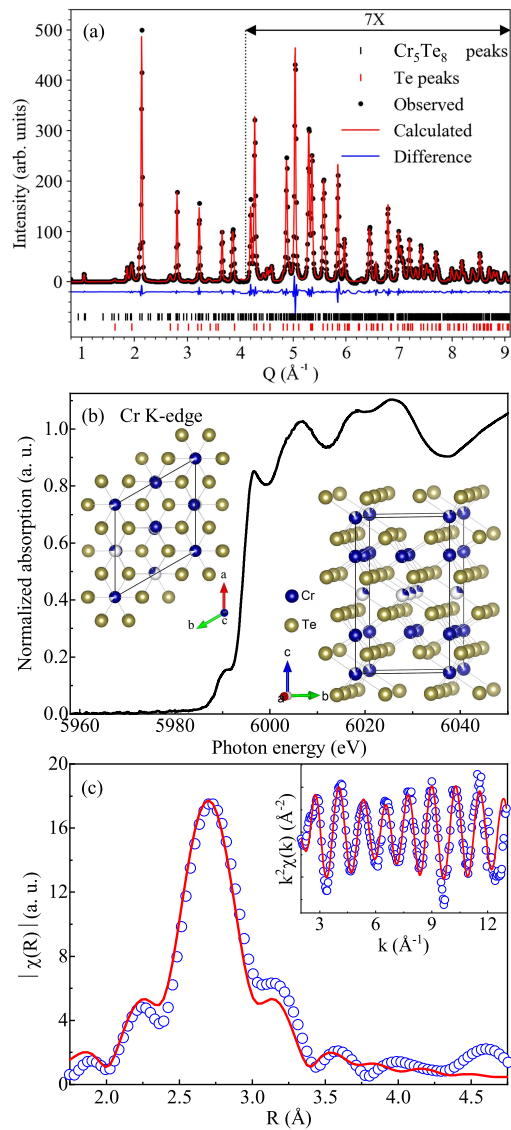


FIG. 1. (Color online). (a) Refinement of synchrotron x-ray diffraction data of Cr_5Te_8 : data (solid symbols), structural model (red solid line), difference curve (blue solid line, offset for clarity). Vertical tickmarks denote reflections in the main phase (black, top row) and the secondary Te impurity (red, bottom row). (b) Normalized Cr K-edge XANES spectra and (c) Fourier transform magnitudes of EXAFS data of Cr_5Te_8 taken at room temperature. The experimental data are shown as blue symbols alongside the model fit plotted as red line. The inset in (c) shows the corresponding EXAFS oscillation with the model fit.

tances in vacancy-free layers range from 2.701 to 2.805 Å, match well with the reported values for $\text{Cr}_2(\text{Si,Ge})_2\text{Te}_6$ (2.741 - 2.803 Å) and CrTe_3 (2.700 - 2.755 Å).²⁶ However, the Cr-Te bond distances in metal-deficient layers are shorter with values of 2.673 - 2.681 Å. The shortest Te-Te interatomic separations range from 3.664 to 3.779 Å, significantly shorter than the sum of their anionic radii 4.2 Å, indicative of weak bonding interactions

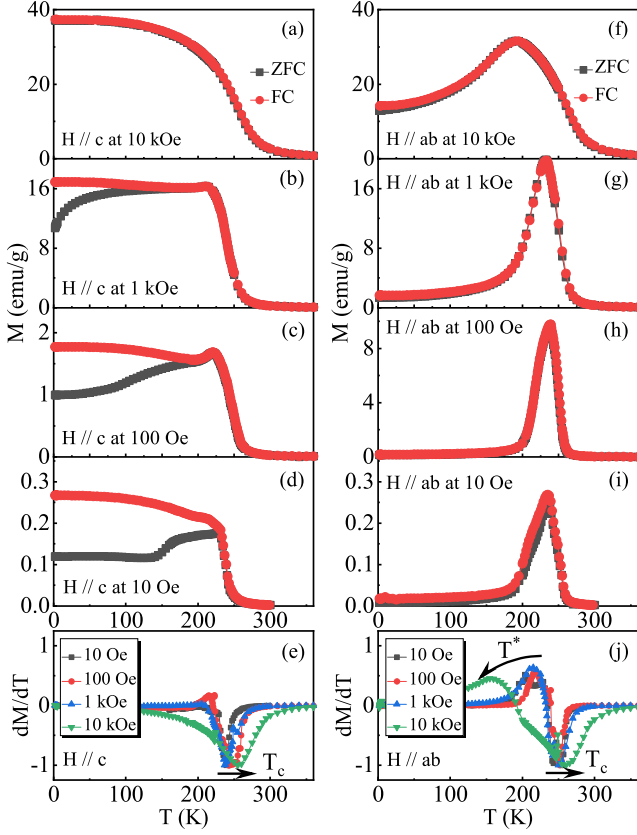


FIG. 2. (Color online). (a)-(d) Temperature dependence of zero field cooling (ZFC) and field cooling (FC) magnetization of Cr_5Te_8 measured at indicated fields applied along the c axis. (e) Temperature-dependent dM/dT derived from FC curves with $\mathbf{H} \parallel c$. (f)-(i) Temperature dependence of ZFC and FC magnetization of Cr_5Te_8 measured at indicated fields applied in the ab plane. (j) Temperature-dependent dM/dT derived from FC curves with $\mathbf{H} \parallel ab$.

with a quasi-2D character.

Figures 1(b) and 1(c) show the normalized Cr K-edge XANES spectra and Fourier transform magnitudes of EXAFS spectra of Cr_5Te_8 , respectively. The XANES spectra is close to that of Cr_2Te_3 with Cr^{3+} state.²⁷ The prepeak feature is due to a direct quadrupole transition to unoccupied $3d$ states that are hybridized with Te p orbitals. In the single-scattering approximation, the EXAFS could be described by the following equation:²⁸

$$\chi(k) = \sum_i \frac{N_i S_0^2}{k R_i^2} f_i(k, R_i) e^{-\frac{2R_i}{\lambda}} e^{-2k^2 \sigma_i^2} \sin[2kR_i + \delta_i(k)],$$

where N_i is the number of neighbouring atoms at a distance R_i from the photoabsorbing atom. S_0^2 is the passive electrons reduction factor, $f_i(k, R_i)$ is the backscattering amplitude, λ is the photoelectron mean free path, δ_i is the phase shift of the photoelectrons, and σ_i^2 is the correlated Debye-Waller factor measuring the mean square relative displacement of the photoabsorber-backscatter pairs. The corrected main peak around $R \sim 2.7 \text{ \AA}$ in

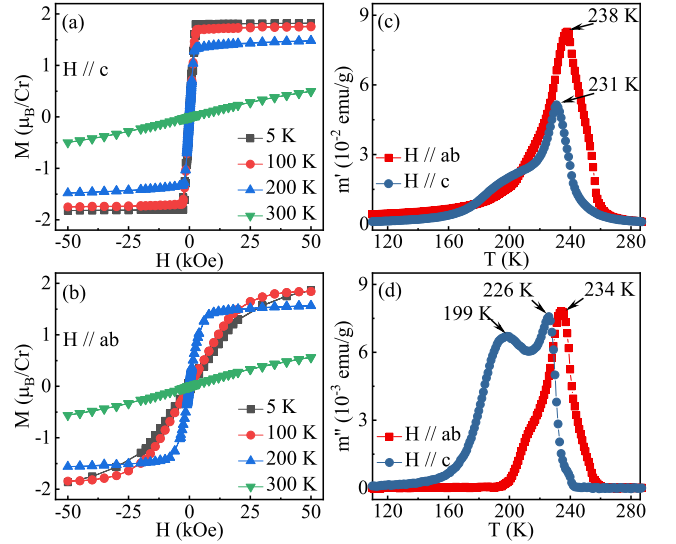


FIG. 3. (Color online). Magnetization as function of field at various temperatures for (a) $\mathbf{H} \parallel c$ and (b) $\mathbf{H} \parallel ab$, respectively. Ac susceptibility real part (c) $m'(T)$ and (d) imaginary part $m''(T)$ as a function of temperature measured with oscillated ac field of 3.8 Oe and frequency of 499 Hz applied in the ab plane and along the c axis, respectively.

Fig. 1(b) corresponds to the Cr-Te bond distances [$\text{Cr}2\text{-Te}1$: 2.70(1) \AA , $\text{Cr}2\text{-Te}4$: 2.74(2) \AA , $\text{Cr}4\text{-Te}2$: 2.683(1) \AA] extracted from the model fit in the range 2 \AA to 3 \AA , only slightly modified when compared with the average bond distances. The peaks in high R range are due to longer Cr-Cr (3.01 $\text{\AA} \sim 3.29 \text{ \AA}$) and Te-Te (3.66 $\text{\AA} \sim 3.78 \text{ \AA}$) bond distances and multiple scattering effects.

Temperature dependence of zero field cooling (ZFC) and field cooling (FC) magnetization $M(T)$ taken at various magnetic fields for Cr_5Te_8 is presented in Fig. 2. We observe an interesting anisotropic magnetic response for fields applied along the c axis and in the ab plane, respectively. In Fig. 2(a), for $\mathbf{H} \parallel c$ at 10 kOe, a typical increase in $M(T)$ on cooling from high temperature corresponds well to the reported paramagnetic (PM) to FM transition.¹⁶ An appreciable thermomagnetic irreversibility occurs between the ZFC and FC curves in lower fields [Figs. 2(b)-2(d)], in the magnetically ordered state, indicating magnetocrystalline anisotropy. On the other hand, for $\mathbf{H} \parallel ab$, an anomalous peak feature is observed. The ZFC and FC magnetization in fields ranging from 10 kOe to 10 Oe are virtually overlapping in the whole temperature range [Figs. 2(f)-2(i)]. A similar magnetization downturn below T_c is also seen for $\text{Cr}_2(\text{Si,Ge})_2\text{Te}_6$ and $\text{Cr}(\text{Br,I})_3$,^{29,30} at which the strong magnetic anisotropy emerges. Since the ZFC curve might be influenced by the domain wall motion, we summarize the field dependence of T_c (the minimum of dM/dT) and T^* (the maximum of dM/dT) from FC magnetization. As shown in Figs. 2(e) and 2(j), both T_c and T^* are field-dependent but with an opposite tendency, i.e., with increasing field the T_c increases whereas the T^* gradually decreases.

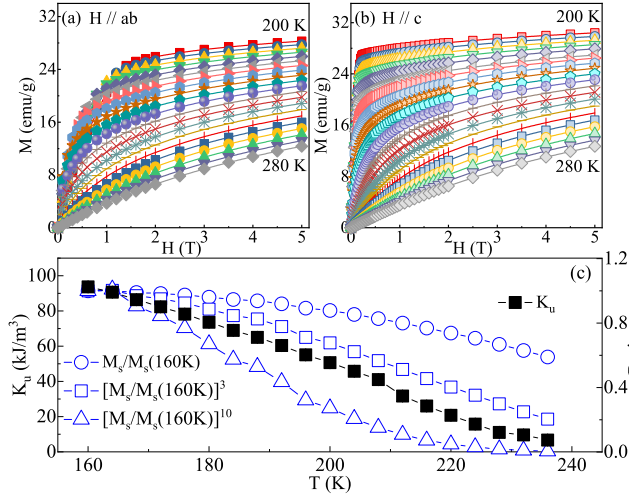


FIG. 4. (Color online). Typical initial isothermal magnetization curves from $T = 200$ K to 280 K with temperature step of 4 K measured (a) in the ab plane and (b) along the c axis, respectively. (c) Temperature-dependent anisotropy constant K_u (left axis) and the ratios of $[M_s/M_s(160K)]^{n(n+1)/2}$ with $n = 1, 2,$ and 4 (right axis).

Isothermal magnetization $M(H)$ for $\mathbf{H} \parallel \mathbf{c}$ exhibits a clear FM behavior at low temperatures and a linear PM behavior with small slope at 300 K [Fig. 3(a)]. The mild hysteresis for both orientations indicates the behavior expected for a soft ferromagnet. The observed saturation magnetization of $M_s \approx 1.8 \mu_B/\text{Cr}$ for $\mathbf{H} \parallel \mathbf{c}$ at 5 K which is smaller when compared to the expected value for Cr free ion ($3 \mu_B/\text{Cr}$), indicating weak itinerant nature of Cr or canted FM in Cr_5Te_8 .¹⁹ The saturation field H_s could be derived from the x component of the intercept of two linear fits, one being a fit to the saturated regime at high fields and one being a fit of the unsaturated linear regime at low fields. As we can see, the magnetization is much easier to saturate for $\mathbf{H} \parallel \mathbf{c}$ [Fig. 3(a)] than for $\mathbf{H} \parallel \mathbf{ab}$ [Fig. 3(b)], indicating that the c axis is the easy magnetization direction. The large disparity of H_s for two orientations can be explained by easy (hard) natures of the domain wall motion along different c (ab) axes. Figures 3(c) and 3(d) present the temperature dependence of ZFC ac susceptibility measured with oscillated ac field of 3.8 Oe and frequency $f = 499$ Hz. A pronounced broad peak is observed at T_c in the real part m' , i. e. at 238 K for $\mathbf{H} \parallel \mathbf{ab}$ and at 231 K for $\mathbf{H} \parallel \mathbf{c}$. An additional anomaly occurs just below T_c , as seen in an obvious hump in the imaginary part m'' at 199 K for $\mathbf{H} \parallel \mathbf{c}$, further confirming the anisotropic magnetic response.

Using the Stoner-Wolfarth model a value for the magnetocrystalline anisotropy constant K_u can be estimated from the saturation regime in the isothermal magnetization curve. Figures 4(a) and 4(b) present the magnetization isotherms with field up to 5 T in the temperature range from 200 to 280 K for both $\mathbf{H} \parallel \mathbf{ab}$ and $\mathbf{H} \parallel \mathbf{c}$.

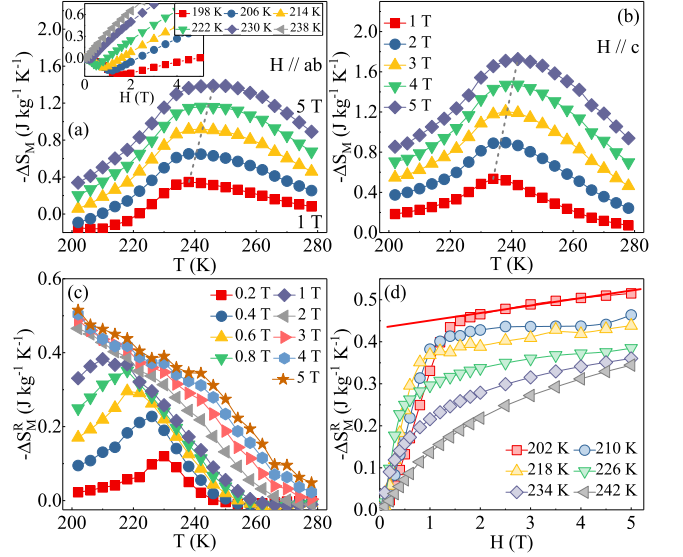


FIG. 5. (Color online). Temperature dependence of magnetic entropy change $-\Delta S_M$ obtained from magnetization measurement at various magnetic field changes (a) in the ab plane and (b) along the c axis, respectively. Inset shows the field dependence of $-\Delta S_M$ at low temperature. The rotational magnetic entropy change $-\Delta S_M^R$ as a function of (c) temperature and (d) field.

When $\mathbf{H} \parallel \mathbf{ab}$, where the anisotropy becomes maximal, the saturation field H_s is associated with the magnetocrystalline anisotropy constant K_u and the saturation magnetization M_s with μ_0 being the vacuum permeability: $2K_u/M_s = \mu_0 H_s$.³¹ Figure 4(c) exhibits the temperature dependence of derived K_u for Cr_5Te_8 , which is about 94 kJ cm^{-3} at $T = 160$ K. The K_u in Cr_5Te_8 is larger than those for $\text{Cr}_2(\text{Si,Ge})_2\text{Te}_6$ and CrBr_3 ,^{22,30} which most likely results in a more apparent magnetization downturn anomaly in Cr_5Te_8 [Figs. 2(f)-2(i)]. Here we propose that the origin of this downturn in the magnetization curve for $\mathbf{H} \parallel \mathbf{ab}$ is a continuous reorientation of the magnetization direction as a result of an interplay between the magnetocrystalline anisotropy, field and temperature. The magnetocrystalline anisotropy favors a magnetization direction perpendicular to the ab plane, which for $\mathbf{H} \parallel \mathbf{ab}$ the field wants to align the magnetization direction parallel to the field. Assuming an external field H_1 is higher than the anisotropy field H^* at temperature T_1 below T^* , the magnetization vector is aligned along the external field direction. By reducing the external field to a value H_2 below H^* at fixed T_1 , a tilting of the magnetization vector towards the easy c axis will be achieved. The tilting in turn leads to a reduction of the magnetization component parallel to the field. This is like the spin-flop mechanism that usually is observed in an AFM ordered state. Such feature is also presented in the field-dependent magnetization in the hard ab plane [Fig. 3(b)] at 5 and 100 K.

Furthermore, the magnetocrystalline anisotropy K_u for Cr_5Te_8 is found to be temperature-dependent [Fig. 4(c)],

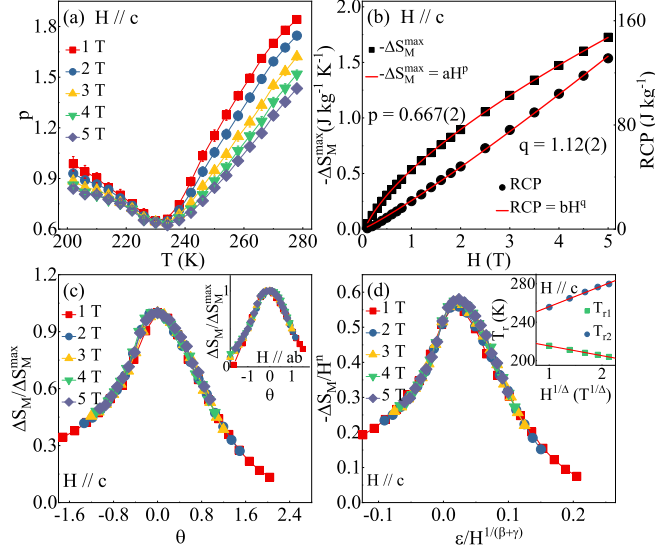


FIG. 6. (Color online). (a) Temperature dependence of p in various fields. (b) Field dependence of the maximum magnetic entropy change $-\Delta S_M^{\max}$ and the relative cooling power RCP with power law fitting in red solid lines. (c) The normalized ΔS_M as a function of the rescaled temperature θ with out-of-plane field and in-plane field (inset). (d) Scaling plot of ΔS_M based on the critical exponents $\beta = 0.315$ and $\gamma = 1.81$.¹⁹ Inset shows T_r vs $H^{1/\Delta}$ with $\Delta = \beta + \gamma$.

gradually increasing with decreasing temperature. This tendency arises solely from a large number of local spin clusters fluctuating randomly around the macroscopic magnetization vector and activated by a nonzero thermal energy.^{32,33} In a simple classical theory, $\langle K^{(n)} \rangle \propto M_s^{n(n+1)/2}$, where $\langle K^{(n)} \rangle$ is the anisotropy expectation value for the n^{th} power angular function,^{32,33} in the case of uniaxial anisotropy $n = 2$ and of cubic anisotropy $n = 4$, leading to an exponent of 3 and 10, respectively. The temperature-dependent $M_s/M_s(160\text{K})$, $[M_s/M_s(160\text{K})]^3$, and $[M_s/M_s(160\text{K})]^{10}$ are also plotted. The comparison in Fig. 5(c) points to the predominant uniaxial anisotropy with some deviation to cubic anisotropy in Cr_5Te_8 . As discussed above, reducing the external field from H_1 passing H^* to H_2 at T_1 ($< T^*$) results in a tilting of the magnetization vector towards the easy c axis. The observed temperature-dependent K_u gives a reduction of magnetic anisotropy when increasing temperature to T_2 ($> T^*$). Then the alignment along the magnetic easy axis becomes less favorable upon warming, which leads to a stronger tilting of the magnetization vector towards the ab plane and an increased experimentally observed ab -component magnetization. Therefore, the spin configuration of Cr_5Te_8 below T_c is supposed to be an out-of-plane FM order with in-plane AFM components, calling for further neutron scattering measurement. This canted FM configuration might arise from the ordered Cr-vacancies induced modification of local structure and indicates competing exchange interactions

exist in Cr_5Te_8 .

To further characterize the anisotropic magnetic properties in Cr_5Te_8 , we investigate the anisotropic magnetic entropy change:

$$\Delta S_M(T, H) = \int_0^H \left(\frac{\partial S}{\partial H} \right)_T dH = \int_0^H \left(\frac{\partial M}{\partial T} \right)_H dH,$$

where $\left(\frac{\partial S}{\partial H} \right)_T = \left(\frac{\partial M}{\partial T} \right)_H$ is based on Maxwell's relation.³⁴ In the case of magnetization measured at small discrete field and temperature intervals,

$$\Delta S_M(T_i, H) = \frac{\int_0^H M(T_i, H) dH - \int_0^H M(T_{i+1}, H) dH}{T_i - T_{i+1}}.$$

Figures 5(a) and 5(b) show the calculated $-\Delta S_M(T, H)$ as a function of temperature in selected fields up to 5 T with a step of 1 T applied in the ab plane and along the c axis, respectively. All the $-\Delta S_M(T, H)$ curves feature a broad peak in the vicinity of T_c . The value of $-\Delta S_M$ increases monotonically with increasing field; the maximal value reaches $1.39 \text{ J kg}^{-1} \text{ K}^{-1}$ in the ab plane and $1.73 \text{ J kg}^{-1} \text{ K}^{-1}$ along the c axis, respectively, with field change of 5 T. Most importantly, the values of $-\Delta S_M$ for the ab plane are negative at low temperatures in low fields, however, all the values are positive along the c axis. The field dependence of $-\Delta S_M(T, H)$ at low temperature [inset in Fig. 5(a)] shows a clear sign change for $\mathbf{H} \parallel \mathbf{ab}$. This behavior is similar with that in CrI_3 ,²³ in which the magnetic anisotropy originates mainly from the superexchange interaction.³⁵ The calculated magnetocrystalline anisotropy decreases with increasing temperature [Fig. 4(c)], whereas the magnetization may exhibit opposite behavior. At low fields, the magnetization at higher temperature could be larger than that at lower temperature [Figs. 2(f)-(i) and 3(b)], which gives a negative $-\Delta S_M$. The rotational magnetic entropy change ΔS_M^R can be calculated as $\Delta S_M^R(T, H) = \Delta S_M(T, H_c) - \Delta S_M(T, H_{ab})$. As shown in Fig. 5(c), the temperature dependence of $-\Delta S_M^R(T, H)$ also features a peak at T_c with the field change of 0.2 T, however, the temperature of the maximum $-\Delta S_M^R(T, H)$ moves away from T_c to lower temperature with increasing field. When $T \leq T_c$, the field dependence of $-\Delta S_M^R(T, H)$ increases rapidly at low field and changes slowly at high field [Fig. 5(d)]. This possibly reflects the anisotropy field in Cr_5Te_8 , which decreases with increasing temperature and gradually disappears when $T \geq T_c$. The obtained $-\Delta S_M$ of Cr_5Te_8 is significantly smaller than those of well-known magnetic refrigerating materials, such as $\text{Gd}_5\text{Si}_2\text{Ge}_2$, $\text{LaF}_{13-x}\text{Si}_x$, and $\text{MnP}_{1-x}\text{Si}_x$,³⁶ however, comparable with those of $\text{Cr}(\text{Br},\text{I})_3$ and $\text{Cr}_2(\text{Si},\text{Ge})_2\text{Te}_6$.^{22,37,38}

For a material displaying a second-order transition,³⁹ the field-dependent maximum magnetic entropy change should be $-\Delta S_M^{\max} \propto H^p$.⁴⁰ Another important parameter is the relative cooling power $RCP = -\Delta S_M^{\max} \times \delta T_{FWHM}$.⁴¹ The $-\Delta S_M^{\max}$ is the maximum entropy change near T_c and δT_{FWHM} is the full-width at half maximum of $-\Delta S_M$. The RCP also depends on the field

with $RCP \propto H^q$. Figure 6(a) displays the temperature dependence of $p(T)$ in various out-of-plane fields. At low temperatures, well below T_c , p has a value which tends to 1. On the other side, well above T_c , p approaches 2 as a consequence of the Curie-Weiss law. At $T = T_c$, p reaches a minimum. Figure 6(b) summarized the field dependence of $-\Delta S_M^{max}$ and RCP. The RCP is calculated as 131.2 J kg^{-1} with out-of-plane field change of 5 T for Cr_5Te_8 , which is comparable with that of CrI_3 (122.6 J kg^{-1} at 5 T).²³ Fitting of the $-\Delta S_M^{max}$ and RCP gives $p = 0.667(2)$ and $q = 1.12(2)$.

Scaling analysis of $-\Delta S_M$ can be built by normalizing all the $-\Delta S_M$ curves against the respective maximum $-\Delta S_M^{max}$, namely, $\Delta S_M/\Delta S_M^{max}$ by rescaling the reduced temperature θ_{\pm} as defined in the following equations,⁴²

$$\theta_- = (T_{peak} - T)/(T_{r1} - T_{peak}), T < T_{peak},$$

$$\theta_+ = (T - T_{peak})/(T_{r2} - T_{peak}), T > T_{peak},$$

where T_{r1} and T_{r2} are the temperatures of two reference points that corresponds to $\Delta S_M(T_{r1}, T_{r2}) = \frac{1}{2}\Delta S_M^{max}$. Following this method, all the $-\Delta S_M(T, H)$ curves in various fields collapse into a single curve [Fig. 6(c) and inset]. The values of T_{r1} and T_{r2} depend on $H^{1/\Delta}$ with $\Delta = \beta + \gamma$ [inset in Fig. 6(d)].⁴² In the phase transition region, the scaling analysis of $-\Delta S_M$ can also be expressed as $-\Delta S_M/a_M = H^n f(\varepsilon/H^{1/\Delta})$, where $a_M = T_c^{-1}A^{\delta+1}B$ with A and B representing the critical amplitudes as in $M_s(T) = A(-\varepsilon)^\beta$ and $H = BM^\delta$, respectively, and $f(x)$ is the scaling function.⁴³ If the critical exponents are appropriately chosen, the $-\Delta S_M(T)$ curves should be rescaled into a single curve, consistent with normalizing all the $-\Delta S_M$ curves with two reference temperatures (T_{r1} and T_{r2}). This is indeed seen in Fig. 6(d) by using the values of $\beta = 0.315$ and $\gamma = 1.81$,¹⁹ confirming that the critical exponents for Cr_5Te_8 are intrinsic and accurately estimated. As is well known, the critical exponents $\beta = 0.25$, $\gamma = 1.75$ and $\beta = 0.325$, $\gamma = 1.24$ are

expected for 2D and 3D Ising models, respectively. The spatial dimension extends from $d = 2$ to $d = 3$ passing through T_c confirms that trigonal Cr_5Te_8 features quasi-2D character. The spin dimension of Ising-type $n = 1$ implies strong uniaxial magnetic anisotropy, which is of high interest for establishing long-range magnetism down to 2D limit.⁴⁴

IV. CONCLUSIONS

In summary, we have studied in detail the anisotropy of magnetic and magnetocaloric properties of trigonal Cr_5Te_8 with a high- T_c of 230 K. A satellite transition T^* is confirmed below T_c , featuring an anomalous magnetization downturn when low field applying in the hard ab plane. A canted out-of-plane FM configuration with in-plane AFM components is supposed for Cr_5Te_8 , suggesting the existence of competing exchange interactions. Intrinsic magnetocrystalline anisotropy in trigonal Cr_5Te_8 is established and also reflected in anisotropic magnetic entropy change. Taken its high- T_c and strong anisotropy, Cr_5Te_8 is a promising material to gain further insight into low-dimensional ferromagnetism and is of high interest or nanofabrication that could led to ferromagnetic heterostructures devices.

ACKNOWLEDGEMENTS

This work was funded by the Computation Material Science Program (Y.L. and C.P.). This research used the 28-ID-1 and 8-ID beamlines of the National Synchrotron Light Source II, a U.S. DOE Office of Science User Facility operated for the DOE Office of Science by Brookhaven National Laboratory under Contract No. de-sc0012704.

¹ N. D. Mermin and H. Wagner, *Phys. Rev. Lett.* **17**, 1133 (1966).

² M. A. McGuire, H. Dixit, V. R. Cooper, and B. C. Sales, *Chem. Mater.* **27**, 612 (2015).

³ B. Huang, G. Clark, E. Navarro-Moratalla, D. R. Klein, R. Cheng, K. L. Seyler, D. Zhong, E. Schmidgall, M. A. McGuire, D. H. Cobden, W. Yao, D. Xiao, P. Jarillo-Herrero, and X. D. Xu, *Nature* **546**, 270 (2017).

⁴ K. L. Seyler, D. Zhong, D. R. Klein, S. Guo, X. Zhang, B. Huang, E. Navarro-Moratalla, L. Yang, D. H. Cobden, M. A. McGuire, W. Yao, D. Xiao, P. Jarillo-Herrero, and X. D. Xu, *Nature Physics* **14**, 277 (2018).

⁵ Z. Fei, B. Huang, P. Malinowski, W. Wang, T. Song, J. Sanchez, W. Yao, D. Xiao, X. Zhu, A. May, W. Wu, D. Cobden, Jiun-Haw Chu, and X. D. Xu, arXiv:1803.02559.

⁶ C. Gong, L. Li, Z. L. Li, H. W. Ji, A. Stern, Y. Xia, T. Cao, W. Bao, C. Z. Wang, Y. Wang, Z. Q. Qiu, R. J. Cava, S. G. Louie, J. Xia, and X. Zhang, *Nature* **546**, 265 (2017).

⁷ M. W. Lin, H. L. Zhuang, J. Q. Yan, T. Z. Ward, A. A. Puzos, C. M. Rouleau, Z. Gai, L. B. Liang, V. Meunier, B. G. Sumpter, P. Ganesh, P. R. C. Kent, D. B. Geohegan, D. G. Mandrus, and K. Xiao, *J. Mater. Chem. C* **4**, 315 (2016).

⁸ H. L. Zhuang, Y. Xie, P. R. C. Kent, and P. Ganesh, *Phys. Rev. B* **92**, 035407 (2015).

⁹ H. Ipser, K. L. Komarek, and K. O. Klepp, *J. Less-Common Met.*, **92**, 265 (1983).

¹⁰ G. B. Street, E. Sawatzky, and K. Lee, *J. Phys. Chem. Solids*, **34**, 1453 (1973).

¹¹ M. Akram, and F. M. Nazar, *J. Mater. Sci.*, **18**, 423 (1983).

- ¹² Z. L. Huang, W. Bensch, S. Mankovsky, S. Polesya, H. Ebert, and R. K. Kremer, *J. Solid State Chem.*, **179**, 2067 (2006).
- ¹³ Z. L. Huang, W. Kockelmann, M. Telling, and W. Bensch, *Solid State Sci.*, **10**, 1099 (2008).
- ¹⁴ A. F. Andresen, *Acta Chem. Scand.*, **24**, 3495 (1970).
- ¹⁵ K. Shimada, T. Saitoh, H. Namatame, A. Fujimori, S. Ishida, S. Asano, M. Matoba, and S. Anzai, *Phys. Rev. B*, **53**, 7673 (1996).
- ¹⁶ K. Lukoschus, S. Kraschinski, C. Näther, W. Bensch, and R. K. Kremer, *J. Solid State Chem.*, **177**, 951 (2004).
- ¹⁷ X. Zhang, T. Yu, Q. Xue, M. Lei, and R. Jiao, *J. Alloys Compd.* **750**, 798 (2018)
- ¹⁸ X. Luo, W. Ren, and Z. Zhang, *J. Magn. Magn. Mater.* **445**, 37 (2018).
- ¹⁹ Y. Liu and C. Petrovic, *Phys. Rev. B* **96**, 134410 (2017).
- ²⁰ Y. Liu and C. Petrovic, *Phys. Rev. B* **98**, 195122 (2018).
- ²¹ Y. Wang, J. Yan, J. Li, S. Wang, M. Song, J. Song, Z. Li, K. Chen, Y. Qin, L. Ling, H. Du, L. Cao, X. Luo, Y. Xiong, and Y. Sun, *Phys. Rev. B* **100**, 024434 (2019).
- ²² Y. Liu and C. Petrovic, *Phys. Rev. Mater.* **3**, 014001 (2019).
- ²³ Y. Liu and C. Petrovic, *Phys. Rev. B* **97**, 174418 (2018).
- ²⁴ A. P. Hammersley, S. O. Svenson, M. Hanfland, and D. Hauserman, *High Pressure Res.* **14**, 235 (1996).
- ²⁵ B. H. Toby and R. B. Von Dreele, GSAS-II: the genesis of a modern open-source all purpose crystallography software package, *Journal of Applied Crystallography*, **46**, 544-549 (2013).
- ²⁶ W. Bensch, O. Helmer, and C. Näther, *Mater. Res. Bull.* **32**, 305 (1997).
- ²⁷ H. Ofuchi, N. Ozaki, N. Nishizawa, H. Kinjyo, S. Kuroda, and K. Takita, *AIP Conference Proceeding* **882**, 517 (2017).
- ²⁸ R. Prins and D. C. Koningsberger (eds.), *X-ray Absorption: Principles, Applications, Techniques of EXAFS, SEXAFS, XANES* (Wiley, New York, 1988).
- ²⁹ L. D. Casto, A. J. Clune, M. O. Yokosuk, J. L. Musfeldt, T. J. Williams, H. L. Zhuang, M. W. Lin, K. Xiao, R. G. Hennig, B. C. Sales, J. Q. Yan, and D. Mandrus, *APL Mater.* **3**, 041515 (2015).
- ³⁰ N. Richter, D. Weber, F. Martin, N. Singh, U. Schwingenschlögl, B. V. Lotsch, and M. Kläui, *Phys. Rev. Mater.* **2**, 024004 (2018).
- ³¹ B. D. Cullity and C. D. Graham, *Introduction to Magnetic Materials* (Wiley, Hoboken, NJ, 2009).
- ³² C. Zener, *Phys. Rev.* **96**, 1335 (1954).
- ³³ W. J. Carr, *J. Appl. Phys.* **29**, 436 (1958).
- ³⁴ V. Pecharsky, K. Gscheidner, *J. Magn. Magn. Mater.* **200**, 44 (1999).
- ³⁵ J. L. Lado and J. F. Rossier, *2D Mater.* **4**, 035002 (2017).
- ³⁶ K. A. Jr Gschneidner, V. K. Pecharsky, and A. O. Tsokol, *Rep. Prog. Phys.* **68**, 1479 (2005).
- ³⁷ X. Y. Yu, X. Zhang, Q. Shi, S. J. Tian, H. C. Lei, K. Xu, and H. Hosono, *Front. Phys.* **14**, 43501 (2019).
- ³⁸ Y. Sun and X. Luo, *Phys. Status Solidi B* (2019) 1900052.
- ³⁹ H. Oesterreicher and F. T. Parker, *J. Appl. Phys.* **55**, 4334 (1984).
- ⁴⁰ V. Franco, J. S. Blazquez, and A. Conde, *Appl. Phys. Lett.* **89**, 222512 (2006).
- ⁴¹ K. A. Gschneidner Jr., V. K. Pecharsky, A. O. Pecharsky, and C. B. Zimm, *Mater. Sci. Forum* **315-317**, 69 (1999).
- ⁴² V. Franco and A. Conde, *Int. J. Refrig.* **33**, 465 (2010).
- ⁴³ Y. Su, Y. Sui, J. G. Cheng, J. S. Zhou, X. Wang, Y. Wang, and J. B. Goodenough, *Phys. Rev. B* **87**, 195102 (2013).
- ⁴⁴ Y. Liu, L. Wu, X. Tong, J. Li, J. Tao, Y. Zhu and C. Petrovic, *Sci. Rep.* **9**, 13599 (2019).